Study of cation distribution, structural and electrical properties of Al–Zn substituted Ni–Co ferrite

Vinod Tukaram [a], S.S. Shinde [b], Rameshwar B. Borade [a], Ankush B. Kadam [a,*]

[a] Jawahar Arts, Science and Commerce College, Andur, Tuljapur, Osmanabad, Maharashtra, 413603, India
[b] Arts, Science and Commerce College, Naldurg, Tuljapur, Osmanabad, Maharashtra, 413602, India

ABSTRACT

In the present study, Nanocrystalline $Ni_{0.5-x}Zn_xCo_{0.5}Fe_{2-y}Al_yO_4$ ($0 \leq x \leq 0.5$ and $0 \leq y \leq 1.0$) powders were fabricated via the sol-gel auto-combustion route. X-ray diffraction study revealed that the formation of single-phase Al–Zn substituted Ni–Co ferrites which have a cubic spinel structure. The lattice parameter shows a decreasing trend from 8.344 to 8.289 Å with the composition of Al^{3+}-Zn^{2+}. The range of crystallite size calculated from the Scherer formula is 46–6.9 nm. Cation distribution indicates that Zn^{2+} strongly occupies tetrahedral A-site and Al^{3+} ions occupied both tetrahedral A-site and octahedral B-site for all composition. Using the vibrating sample magnetometer, it is observed that the Coercive field (Hc), saturation magnetization (Ms), rotational permeability (μ_{rk}), anisotropy field (Ha) and anisotropy constant (K_1) decreases with increasing the composition of Al^{3+}-Zn^{2+}. Fabricated samples show normal dielectric behavior and dielectric constant is increased with an increase of Al–Zn concentration.

1. Introduction

Spinel ferrites having the general formula MFe_2O_4 have more attracted because of their wide range of promising technological applications such as memory storage devices, catalysis, gas sensors, magnetic drug delivery, medical diagnostics, microwave devices, magnetic recording, and electronic industries [1]. The characteristics of ferrites samples depend on the method of synthesis, composition, cation distribution, and microstructure of the samples [2,3]. There are several different synthesis methods used to prepare the ferrites as noted in the previous novels containing citrate gel auto-combustion method, mechano-chemical co-precipitation, and hydrothermal [4,5]. The magnetic parameters of a spinel system are collectively responsive to the synthesis method, types of cation and their occupancy in different sites. The distribution of cation depends on the types of bonding and the ionic radii of the cations. A. Džunuzović et al. [6] fabricated Zn-substituted Ni-ferrites and studied their structural and morphological properties. The results show that Zn-substituted Ni-ferrites are of cubic spinel structure and grain size of samples increases with Zn composition. Charalampos Stergiou [7] reported dielectric and magnetic properties of rare-earth (Y and La) substituted Ni–Co–Zn spinel ferrites. It is observed that dielectric constant is increased with the rare-earth substitution due to the improvement of the dielectric orientation polarization. D.R.S. Gangaswamy et al. [8] fabricated Co-substituted Ni–Zn–Mg ferrite and investigated the magnetic properties. It is found that saturation magnetization is decreased and soft magnetic nature increases with Co substitution. S.J. Haralkar et al. [9] prepared Cr-substituted Mg–Zn ferrite and studied the cation distribution. It is observed that the fraction of Fe ions in octahedral sites decreases and the fraction Cr ions in octahedral sites increase with the substitution of Cr. Yu Gao et al. [10] synthesized Li-substituted Ni–Zn ferrite and investigated elastic, structural and magnetic properties. They observed that the characteristic band of ferrite shift towards lower frequency with Li.

Different ions substituted ferrites have been reported in literature very few of them are given above but Ni–Zn–Co–Al is still not fabricated and studied. In this research, we have reported the synthesis of Ni–Co ferrites by the sol-gel method by doping a portion of nonmagnetic Al–Zn content and studied the effect of concentration of contents on the structure, cation distribution, and electrical properties. The cosubstitution of Al–Zn has a strong effect on the structural and magnetic properties of Ni–Co ferrites as compared to their individual substitution. Our main objective is to synthesize hard magnetic material and reduce magnetization by doping non-magnetic Al–Zn ions because materials whose magnetization is low, applicable for the optoelectronic-
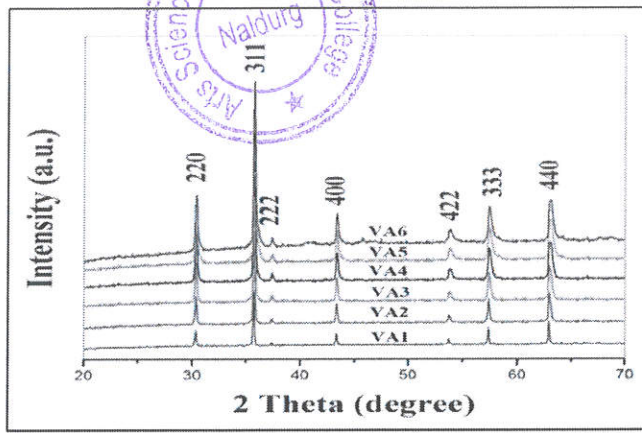
Fig. 1. XRD patterns of $Ni_{0.5-x}Zn_xCo_{0.5}Fe_{2-y}Al_yO_4$.

communication industries.

2. Experimental procedure

Nanocrystalline Al–Zn doped Ni–Co ferrites were fabricated by the sol-gel auto-combustion route with different composition of x and y (x = 0.0, 0.1, 0.2, 0.3, 0.4, 0.5 and y = 0.0, 0.2, 0.4, 0.6, 0.8, 1.0). Analytical grade nitrates and citric acid were used as starting materials to fabricate the $Ni_{0.5-x}Zn_xCo_{0.5}Fe_{2-y}Al_yO_4$ ferrites. The metal nitrates [Fe$(NO_3)_3$·$9H_2O$], [Ni$(NO_3)_2$·$6H_2O$], [Co$(NO_3)_2$·$6H_2O$], [Zn$(NO_3)_2$·$6H_2O$], [Al$(NO_3)_3$·$9H_2O$], and citric acid ($C_6H_8O_7$·H_2O) were weighed in proper stoichiometric molar ratio and dissolved in minimum amount of distilled water. This mixture was mixed thoroughly by stirred on a magnetic hot plate. The pH value was adjusted by using dilute ammonia solution and it is maintained at 7 for all the samples. This mixture was slowly heated and stirred until it turns into a dark viscous gel. The viscous gel solution was dried for self-ignition of gel and conversion into loose powder. All the samples were annealed at 800 °C for 4 h.

Phase analysis and crystallographic properties of prepared samples were studied by XRD analysis and data collected from Philips X-ray diffractometer (PANLYTICAL, Almelo, The Netherlands) with CuKα radiation source (λ = 1.5405 Å). The vibrating sample magnetometry (VSM) was used to record the M − H loop and study the magnetic properties. The IR spectra within the range of 4000–400 cm^{-1} were recorded by Bruker Equinox FTIR spectrophotometer and LCR-Q meter was used to study the dielectric properties.

3. Results and discussions

3.1. Structural analysis

The XRD patterns of simultaneous Al–Zn-substituted Ni–Co ferrites nanoparticles annealed at 800 °C are shown in Fig. 1. The samples are coded as VA1, VA2, VA3, VA4, VA5 and VA6 for the composition of x = 0.0; y = 0.0, x = 0.1; y = 0.2, x = 0.2; y = 0.4, x = 0.3; y = 0.6, x = 0.4; y = 0.8 and x = 0.5; y = 1.0 respectively. All the planes observed in fabricated samples are a good agreement with planes of Ni–Zn–Co

reported earlier [11]. The absence of any other peak exhibits the evolution of single-phase Al–Zn substituted Ni–Co ferrite which has a cubic spinel structure. The lattice constant 'a' was measured using the relation [4].

$$a = d\sqrt{h^2 + k^2 + l^2} \qquad (1)$$

It is observed that 'a' decreases from 8.344 Å to 8.289 Å as the Al^{3+}-Zn^{2+} ions substitution increases. The Zn^{2+} and Al^{3+} are preferentially occupying on A and B sites by replacing Ni^{2+} and Fe^{3+} ions. It is found that Zn^{2+} ions are preferred the tetrahedral sites, whereas Al^{3+} ions are preferred to occupy the tetrahedral and octahedral sites [12]. This can be related to the fact that the ionic radius of Al^{3+} ions (0.51 Å) is smaller as compared to that of Fe^{3+} ions (0.67 Å). The lattice constant does not substantially depend on the substitution of Zn^{2+} ions due to the small difference between the ionic radii of Zn^{2+} ions (0.74 Å) and Ni^{2+} ions (0.72 Å). Also, the composition of Al^{3+} ions is larger than Zn^{2+} ions. When the larger Fe^{3+} ions were replaced by the smaller Al^{3+} ions, the unit cell shrinking while preserving the overall cubic symmetry. The most intense peak (311) was used to calculate the crystallite size for all the compositions using Scherer Formula [13]:

$$D = \frac{0.9\lambda}{\beta \ Cos\theta} \qquad (2)$$

The values of crystallite size (D) are estimated within the range of 46–6 nm (Table 1) and it decreases with increasing Al^{3+}-Zn^{2+} ions substitution.

The strain (ε) induced in the nanocrystals were computed with the help of relation:

$$\varepsilon = \frac{\beta}{4\tan\theta} \qquad (3)$$

The dislocation density (δ) was calculated using the relation [14]:

$$\delta = \frac{1}{D^2} \qquad (4)$$

The packing factor (P) was calculated to enlighten the difference in the strain and dislocation density [15]:

$$P = \frac{D}{d} \qquad (5)$$

where d is interplanar spacing. The values of strain induced in a crystal are increases up to the x = 0.3, y = 0.6 after that it shows slow decreasing trend with the increase of Al–Zn substitution in Ni–Co ferrite. This is due to the difference in ionic radii and the simultaneous substitution of Al and Zn. Values of strain and dislocation density are increased with increasing Al–Zn concentration (Table 1), which indicates the concentration of lattice imperfections, is increasing. This is due to the enhancement of grain boundaries because of the decrease in the crystallite size of ferrite samples. The density of material is more influenced by the molecular weight of that material. It is observed that the molecular weights of the samples are increased with Al–Zn composition. Also, dislocation density is inversely proportional to the crystallite size. The packing factor decreases (Table 1) with increasing Al–Zn substitution in place of iron and nickel is due to the increasing density of the samples.

Table 1
Lattice constant (a), Particle size (D), Strain (ε), Dislocation density (δ), Packing factor (p) of $Ni_{0.5-x}Zn_xCo_{0.5}Fe_{2-y}Al_yO_4$.

Sr. No.	Code	Sample	a (Å)	D(nm)	strain (ε) x 10^{-3}	dislocation density (δ) (g/m^3)	Packing factor (p)
1	VA1	x = 0, y = 0	8.344	46.72	157.3	6.055	18.53
2	VA2	x = 0.1, y = 0.2	8.332	30.56	157.9	9.305	12.14
3	VA3	x = 0.2, y = 0.4	8.327	23.53	158.7	12.15	9.375
4	VA4	x = 0.3, y = 0.6	8.318	19.85	158.9	14.44	7.914
5	VA5	x = 0.4, y = 0.8	8.309	7.315	158.8	39.19	2.915
6	VA6	x = 0.5, y = 1.0	8.289	6.9	157.0	41.20	2.734

Table 2
Cation distribution and Intensity ratio calculations for $Ni_{0.5-x}Zn_xCo_{0.5}Fe_{2-y}Al_yO_4$.

Sample	Cation Distribution		Intensity ratios				Agreement Factor	
	A-site	B-site	(220/400)		(422/400)		(220/400)	(422/400)
			Obs.	Cal.	Obs.	Cal.		
VA1	$Ni_{0.1}Fe_{0.9}$	$Ni_{0.4}CO_{0.5}Fe_{1.1}$	1.310	1.352	0.801	0.738	−0.042	0.063
VA2	$Ni_{0.05}Zn_{0.1}Al_{0.1}Fe_{0.75}$	$Ni_{0.35}CO_{0.5}Al_{0.1}Fe_{1.05}$	1.262	1.351	0.812	0.782	−0.089	0.030
VA3	$Ni_{0.02}Zn_{0.2}Al_{0.2}Fe_{0.58}$	$Ni_{0.28}CO_{0.5}Al_{0.2}Fe_{1.02}$	1.217	1.367	0.824	0.855	−0.150	−0.031
VA4	$Ni_{0.01}Zn_{0.3}Al_{0.3}Fe_{0.39}$	$Ni_{0.19}CO_{0.5}Al_{0.3}Fe_{1.01}$	1.179	1.387	0.828	0.862	−0.208	−0.034
VA5	$Zn_{0.4}Al_{0.4}Fe_{0.2}$	$Ni_{0.1}CO_{0.5}Al_{0.4}Fe_1$	1.126	1.262	0.838	0.883	−0.136	−0.045
VA6	$Zn_{0.5}Al_{0.5}$	$CO_{0.5}Al_{0.5}Fe_1$	1.080	1.262	0.846	0.883	−0.182	−0.037

Table 3
Values of Oxygen parameter 'u' theoretical lattice constant 'a_{th}' ionic radii (r_A and r_B) radii of tetrahedral-A and octahedral-B site for $Ni_{0.5-x}Zn_xCo_{0.5}Fe_{2-y}Al_yO_4$.

Sr. no.	Sample	u (Å)	a_{th}(Å)	r_A(Å)	r_B(Å)	R_A(Å)	R_B(Å)
1	VA1	0.3843	8.346	0.681	0.709	0.681	0.748
2	VA2	0.3841	8.331	0.675	0.698	0.675	0.747
3	VA3	0.3840	8.328	0.672	0.686	0.672	0.747
4	VA4	0.3840	8.317	0.671	0.673	0.671	0.744
5	VA5	0.3841	8.310	0.67	0.661	0.670	0.741
6	VA6	0.3844	8.290	0.67	0.647	0.670	0.734

Table 4
Variation of site bond lengths and site edges for $Ni_{0.5-x}Zn_xCo_{0.5}Fe_{2-y}Al_yO_4$.

Sr. No.	Sample	d_{AX}(Å)	d_{BX}(Å)	d_{AXE}(Å)	d_{BAX}(Å)	d_{BXEU}(Å)
1	VA1	5.297	2.012	6.116	5.677	2.954
2	VA2	5.285	2.010	6.103	5.673	2.950
3	VA3	5.279	2.010	6.096	5.673	2.948
4	VA4	5.275	2.007	6.091	5.666	2.945
5	VA5	5.270	2.005	6.086	5.658	2.942
6	VA6	5.264	1.997	6.078	5.636	2.935

3.2. Cation distribution

The cation distribution in the present system was determined from the analysis of XRD intensities of most sensitive planes (220), (400) and (440) are considered and calculated value tabulated in Table 2, by using the formula suggested by Buerger [16]:

$$I_{hkl} = |F|^2_{hkl} \ P. \ Lp \qquad (6)$$

where, I- is the relative integrated intensity for (hkl) planes, F-structure factor, P-Multiplicity factor, Lp-Lorenz polarization factor. Multiplicity factors (P) are the number of different planes having the same spacing. Lorenz polarization factor is determined by using the formula [17]:

$$L_p = \frac{1 + Cos^2 2\theta}{sin^2\theta cos\theta} \qquad (7)$$

The atomic scattering factor for various ions was taken from the literature [17]. The value of the cation distribution parameter for which experimental and theoretical intensity ratio agrees closely with each other. The estimated cation distributions are shown in Table 2. It is observed that Zn^{2+} strongly occupies tetrahedral A-site and Co^{2+} occupies octahedral B-site. Ni^{2+} ions occupy both tetrahedral A-site and octahedral B-site but at the higher substitution of Al^{3+}-Zn^{2+} ions, it occupies in octahedral B-site only. Whereas, Fe^{3+} ions show no preference to any site and distributed among the tetrahedral and octahedral sites. Zn^{2+} strongly occupies tetrahedral A-site and Al^{3+} ions occupied both tetrahedral A-site and octahedral B-site for all composition. The theoretical lattice parameter (a_{th}) was determined by equation [18]:

$$a_{th} = \left(\frac{8}{3\sqrt{3}}\right)\left\{[r_A + R_0] + \sqrt{3}\,[r_B + R_0]\right\} \qquad (8)$$

where, r_A and r_B are the radii of the (A) and [B] sites, respectively and r_O is the oxygen parameter (1.38 Å). The obvious agreement between the experimental lattice parameter (a_{exp}) and the theoretically calculated one (a_{th}) suggests a proper estimated cation distribution of the system. It is observed that values of theoretical lattice constant (Table 3) are also decreasing with an increase of Al^{3+}-Zn^{2+} substitution. Using the values of theoretical lattice constant, the radius of oxygen ion $R_O = 1.32$ Å and the ionic radius of tetrahedral A-site in the following expression, the oxygen positional parameter (u) can be given by the equation [18]:
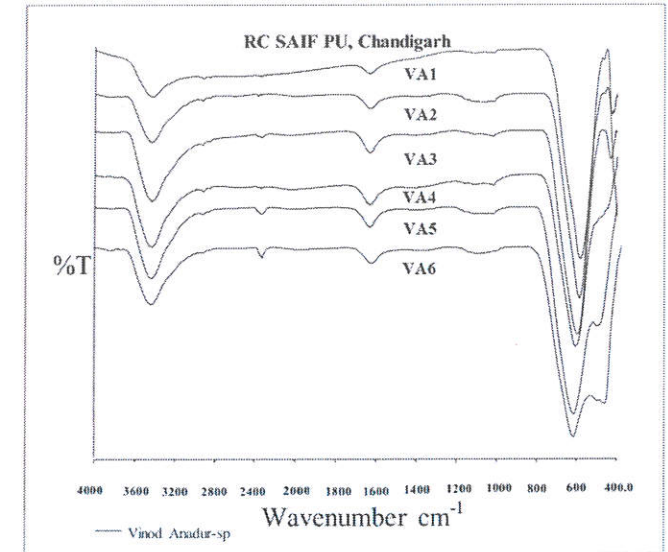
Fig. 2. FT-IR patterns of $Ni_{0.5-x}Zn_xCo_{0.5}Fe_{2-y}Al_yO_4$.

$$u = (r_A + R_0)\frac{1}{a\sqrt{3}} + \frac{1}{4} \qquad (9)$$

It is detected that u (Table 3) is increased with Al^{3+}-Zn^{2+} substitution Ni–Co ferrites which ascribed the increase of 'u' is a direct consequence of increasing the distortion of the A-site oxygen coordination and Al^{3+} ions occupancy by octahedral sites. The bond length of (A) site(d_{AX}), [B] site(d_{BX}), (A) site edge(d_{AXE}) [B] site shared edge(d_{BXE}) and [B] site unshared edge(d_{BXU}) were determined with help of values 'u' and 'a' and equations reported by Jadhav et al. [19]. All the values are presented in Table 4. It is observed that the values of d_{Ax}, d_{Bx}, d_{AXE}, d_{BXEU} and d_{AXE} are decreased with the increasing Al^{3+}-Zn^{2+} substitution. This is because of the difference in ionic radii; the ionic radius of Al^{3+} ions is lower as compared to Fe^{3+} ions.

3.3. Infrared spectroscopy (IR)

Infrared spectra as shown in Fig. 2 were recorded in the frequency range 400–4000 cm^{-1} at room temperature. It is observed from Table 5,

Table 5

IR wavenumber (ν_1, ν_2), tetrahedral k_t, octahedral k_o and Difference between ν_1 and ν_2 of $Ni_{0.5-x}Zn_xCo_{0.5}Fe_{2-y}Al_yO_4$.

Sr. no.	Sample	$\nu_1(cm^{-1})$	$\nu_2(cm^{-1})$	k_t	k_o	ν_1-$\nu_2(cm^{-1})$
1	VA1	575.19	301.24	141492.7	55107.78	273.95
2	VA2	573.83	338.51	135624.2	67744.66	235.32
3	VA3	568.04	380.94	127945.5	83414.12	187.1
4	VA4	569.01	456.17	123550.9	116141.1	112.84
5	VA5	572.86	441.73	120331	105648.6	131.13
6	VA6	577.69	437.84	117460.7	100568.1	139.85
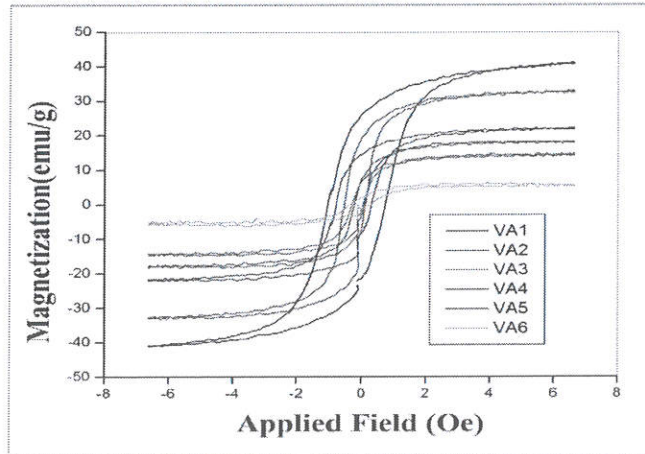
Fig. 3. VSM curve of $Ni_{0.5-x}Zn_xCo_{0.5}Fe_{2-y}Al_yO_4$.

each spectrum exhibit two main absorption bands below $1000\ cm^{-1}$ range which reveals the formation of a single phase of spinel ferrites [20]. The occurrence of the higher frequency band in the range of $583-637\ cm^{-1}$ has been related to the intrinsic vibrations of the tetrahedral complexes, whereas that lower frequency band in the range of $419-485\ cm^{-1}$ is ascribed to the intrinsic vibrations of the octahedral complexes. It explains that the octahedral cluster is lower than the tetrahedral cluster in a normal mode of vibration. It should be ascribed to the longer bond length of the octahedral cluster and shorter bond length of the tetrahedral cluster. It has been seen in the spectrum that the band positions ν_1 and ν_2 change slightly towards higher frequency side with increasing Al^{3+} ions (ionic radius 0.5 Å) which are replacing Fe^{3+} ions (ionic radius of 0.67 Å) at [B] site. Therefore site radius decreases and consequently fundamental frequency increases and hence the central frequency should shift towards the higher frequency side. The displacement of Fe^{3+} ions by smaller Al^{3+} ions decreases the M − O bond length and consequently will increase the wavenumber of ν_2 band. The bands presenting in the range of 3421–3325 and at $1635\ cm^{-1}$ are related H–O–H bending vibration of water molecules.

The force constants related to the (A) and [B] sites were determined by the equations given below [21]:

$$K_t = 7.62 \ \times \ M_1 \ \times \ \vartheta_1^2 \ \times \ 10^{-3}\frac{dyne}{cm} \tag{10}$$

$$K_o = 10.62 \ \times \ \frac{M_2}{2} \ \times \ \vartheta_2^2 \ \times \ 10^{-3}\frac{dyne}{cm} \tag{11}$$

where K_t and K_O are the force constants of (A) and [B] sites, respectively, M_1 is molecular weight of the (A) site, M_2 is molecular weight of the [B] site, absorption peak ν_1 corresponds to a tetrahedral site and ν_2 corresponds to an octahedral site. The cation distribution was used to calculate M_1 and M_2 for each sample. It is observed from Table 5 that the force constants of both (A) and [B] sites are increased with the composition of Al–Zn because of force constants are inversely proportional to the bond length. The difference between ν_1 and ν_2 (as ν_1- ν_2) decreases with increasing Al^{3+}-Zn^{2+} substitution. This indicates that the super-exchange interaction at a and d sites may increase [22], According to theory, the variation of the super-exchange interaction significantly affects the magnetic properties and confirmed also by proposed cation distribution.

3.4. Magnetic properties

Magnetic hysteresis loops were recorded for Al–Zn substituted Ni–Co samples annealed at 800 °C are shown in Fig. 3. The values of Ms decreases with Al–Zn ion content because the ion moment of Al^{3+} ($0\mu_B$) is less than the ion moment of Fe^{3+} ($5\ \mu_B$) in the [B] site of the ferrite sublattice leading to the weakening of A-B interactions. As the concentration of substitution of Al and Zn ions increases for Ni–Co ferrite, Zn is preferred to occupy (A) sites [23], Fe is preferred to occupy both (A) and [B] sites whereas Al and Ni are preferred to occupy [B] sites [24]. Ni replaced by Zn at (A) site due to this Fe^{3+} ion shifts from (A) to [B], hence,'μ_B' of the site [B] increases as compared to (A) site. Therefore, the overall magnetic moment should be increased but on the contrary, the magnetization showed a decreasing trend with Al–Zn substitution. It decreases the Fe^{3+}(B)/Fe^{3+}(A) ratio, resulting in a magnetic moment overall decrease in saturation magnetization. The magnetic parameters collectively depend upon density, porosity, crystallite size, grain size, and A–B superexchange interaction. It is observed that crystallite size is decreased from 46 to 6 nm with increasing Al–Zn substitution due to this saturation magnetization decrease with Al–Zn composition. The saturation magnetization and coercivity values are tabulated in Table 6. The value of coercivity Hc, decreases as the Al^{3+} concentration is increased. This may be attributed to the decrease in anisotropy field, which in turn decreases the domain wall energy with Al–Zn concentration [25,26]. The magnetic moment per formula $[n_B^N]$ is
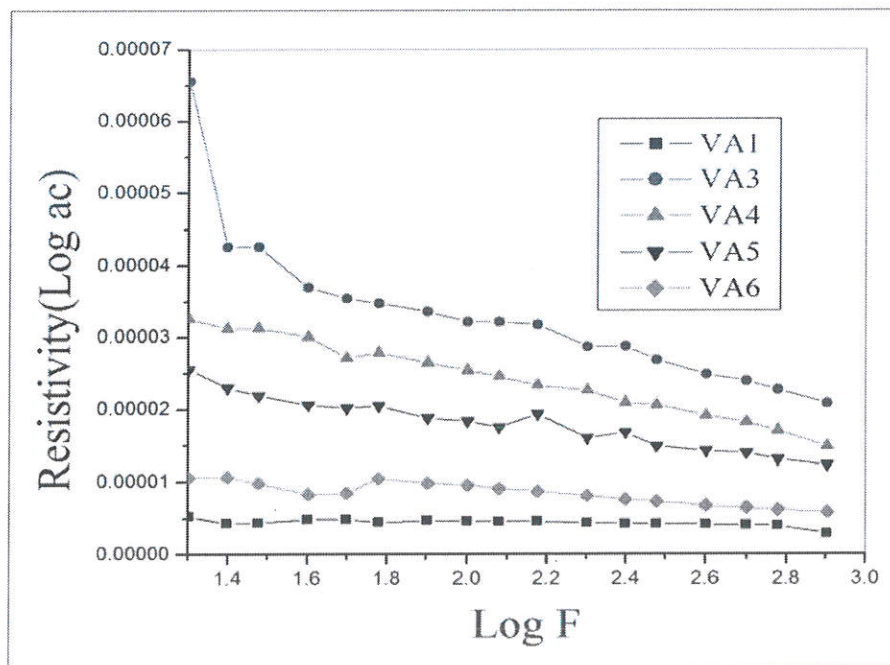
$$n_B^N = M_B - M_A \tag{12}$$

where M_A and M_B are the magnetic moments at (A) and [B]. The calculated values of n_B^N by using the cation distribution and Néel's equation are listed in Table 6. The anisotropy constants are determined by using the values of Hc and Ms by the relation [27]:

Table 6

Saturation magnetization (Ms), Coercive field (Hc), magneton number (n_B), Anisotropy constant (K_1), Rotational permeability (μ_{rk}) and Anisotropy field (Ha) of $Ni_{0.5-x}Zn_xCo_{0.5}Fe_{2-y}Al_yO_4$.

Sr. no.	Sample	Ms (emu/g)	Hc (Oe)	Magneton number $n_B(\mu_B)$		K_1	(μ_{rk})	Ha
				Observed	Neel Model			
1	VA1	41.19	1014.8	1.729	2.1	43541	72917	2114
2	VA2	33.11	670.96	1.360	2.6	23141	38753	1397
3	VA3	22.21	439.04	0.892	3.22	10157	17010	914.6
4	VA4	18.33	224.48	0.756	3.96	4286.1	71779	467.6
5	VA5	14.85	299.6	0.569	4.7	4634.4	77612	624.1
6	VA6	6.3	524.16	0.235	5.5	3439.8	57606	1092
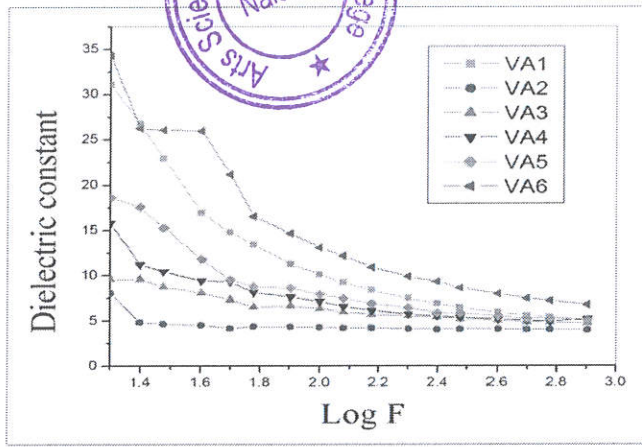
Fig. 4. Dialectical constant ($\dot{\varepsilon}$) of $Ni_{0.5-x}Zn_xCo_{0.5}Fe_{2-y}Al_yO_4$.
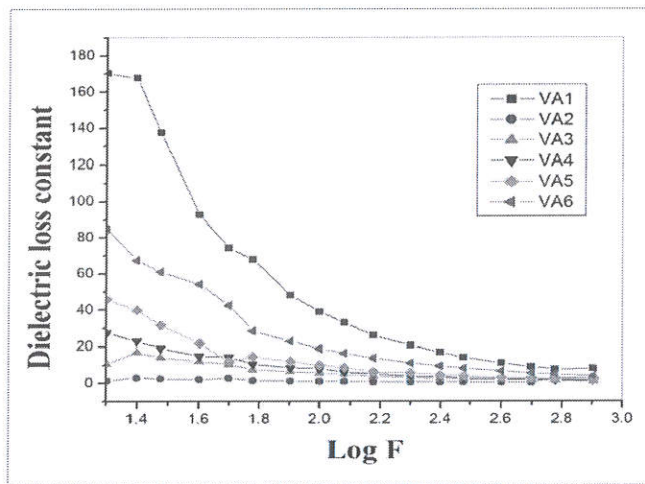
Fig. 5. Dielectric loss constant ($\ddot{\varepsilon}$) $Ni_{0.5-x}Zn_xCo_{0.5}Fe_{2-y}Al_yO_4$.

$$K_1 = \frac{H_c X M_s}{0.96} \tag{13}$$

The anisotropy field (*Ha*) is calculated as per [28] using the relation;

$$H_a = \frac{2K_1}{M_s} \tag{14}$$

The rotational permeability (μ_{rk}) is determined [29] using the relation;

$$\mu_{rk} = 1 + \frac{8\pi M_s}{3H_a} \tag{15}$$

where, *Ms* is the saturation magnetization, K_1 is the anisotropy constant, The calculated values of anisotropy constant, anisotropy field (*Ha*) and rotational permeability (μ_{rk}) are given in Table 6. It is observed that these values are decreased with Al^{3+}-Zn^{3+} ion concentration.

3.5. Electric properties

The pellets of 1 g sample powder were formed by using 5-ton hydraulic pressure and having a diameter of 10 mm and thickness 3 mm. The dielectric constant ($\dot{\varepsilon}$) and loss tangent were determined using the relations [30].

The graph of dielectric constant versus applied frequency is shown in Fig. 4. The dielectric constant ε' is decreased with applied frequency and shows dispersion with frequency. From the graph, it is observed that Al–Zn substituted Ni–Co ferrites have normal dielectric behavior. The dielectric constant is increased with an increase of Al–Zn concentration at room temperature [31]. The dispersion in ε' at lower frequency is according to Maxwell –Wagner interfacial polarization [32,33]. This polarization is as per Koop's Phenomenon logical theory [34]. According to this model, the ferrite sample consists of two-layer dielectric structures, one layer is of well high conducting grains and the other one is poorly conducting grain boundaries. These grain boundaries could be developed at the time of sintering [35]. The number of grain boundaries increases which contributes towards the dielectric constant at lower frequencies while the grains have low dielectric constants is effective at high frequencies. The polarization decreases due to the decreasing the probability of reaching electrons at the grain boundary. They attributed

Fig. 6. AC Resistivity for the samples $Ni_{0.5-x}Zn_xCo_{0.5}Fe_{2-y}Al_yO_4$.

a decrease in ε' is due to the fact that at a certain frequency of external field the electron jumping between Fe^{2+} to Fe^{3+}, cannot follow the AC field [36,36]. The graph of dielectric loss tangent versus log frequency is shown in Fig. 5. The dielectric loss constant is decreased with applied frequency and it is increased with Al–Zn concentration in Ni–Co ferrite.

The graph of AC resistivity versus applied frequency is shown in Fig. 6. All the Al–Zn substituted Ni–Co ferrite samples indicate that ρ_{ac} decreases with an applied frequency which shows the normal behavior of ferrites. From Fig. 6, the resistivity exhibits dispersion at low-frequency and becomes constant at a higher frequency is an agreement with Koops theory. Similar behavior has been shown in the case of other ferrites [37]. This type of variation can be attributed to the variation of ε' and $\tan\delta$ with frequency.

4. Conclusions

Nanocrystalline $Ni_{0.5-x}Zn_xCo_{0.5}Fe_{2-y}Al_yO_4$ ferrite system with different composition of (x = 0.0, 0.1, 0.2, 0.3, 0.4, 0.5 and y = 0.0, 0.2, 0.4, 0.6, 0.8, 1.0), were successfully fabricated by the sol-gel auto-combustion route. The XRD results showed the formation of a cubic spinel structured Al–Zn substituted Ni–Co ferrite. The structural parameters Ni–Co ferrite is increased with the increase of Al–Zn substitution. In FT-IR analysis, there are two peaks around $570\,cm^{-1}$ and $430\,cm^{-1}$ which are characteristic bonds of spinel structure and hence confirm the formation of ferrites. The force constants of the tetrahedral site, K_t, decrease and the octahedral site, K_o, increase with an increase in Al–Zn content. The hysteresis curves of the nanopowders exhibited that the Ms, coercive field, and anisotropy constant decreases whereas rotational permeability increases with the increase of Al–Zn substitution. The magnetization showed a decreasing trend with Al–Zn composition due to reduced AB exchange interactions. The dielectric constant and loss factor of the samples increases with composition due to electron jumping between Fe^{2+} to Fe^{3+}. In this study, samples show excellent properties that have potential uses in optoelectronic-communication industries.

Declaration of competing interest

The authors declare that they have no known competing financial interests or personal relationships that could have appeared to influence the work reported in this paper.

Acknowledgments

References

[1] L.C. Xue, L.Q. Wu, S.Q. Li, Z.Z. Li, G.D. Tang, W.H. Qi, X.S. Ge, L.L. Ding, Physica B 492 (2016) 61–64.

[2] M. Atif, W. Asghar, M. Nadeem, W. Khalid, Z. Ali, S. Badshah, J. Phys. Chem. Solids 123 (2018) 36–42.

[3] Chien-Yie Tsay, Yi-Chun Chiu, Yung-Kuan Tseng, Physica B 570 (2019) 29–34.

[4] Rameshwar B. Borade, Sagar E. Shirsath, Gaurav Vats, Anil S. Gaikwad, S. M. Patange, S.B. Kadam, R.H. Kadam, A.B. Kadam, Nanoscale Adv. 1 (2019) 403–413.

[5] V.K. Mande, D.N. Bhoyar, S.K. Vyawhare, K.M. Jadhav, J. Mater. Sci. Mater. Electron. 29 (2018) 15259–15270.

[6] A. Džunuzović, N. Ilić, M.V. Petrovic, J. Bobic, B. Stojadinović, Z. Dohčević-Mitrović, B. Stojanović, J. Magn. Magn. Mater. 374 (2015) 245–251.

[7] Charalampos Stergiou, J. Magn. Magn. Mater. 426 (2017) 629–635.

[8] D.R.S. Gangaswamy, S. Bharadwaj, M. ChaitanyaVarma, G.S.V.R.K. Choudary, K. H. Rao, J. Magn. Magn. Mater. 468 (2018) 73–78.

[9] S.J. Haralkar, R.H. Kadam, S. S More, Sagar E. Shirsath, M.L. Mane, Swati Patil, D. R. Mane, Physica B 407 (2012) 4338–4346.

[10] Yu Gao, Zhi Wang, Jiajia Pei, Haoming Zhang, J. Alloy. Comp. 774 (2019) 1233–1242.

[11] Ch Srinivas, B.V. Tirupanyam, S.S. Meena, S.M. Yusuf, Ch Seshu Babu, K. S. Ramakrishna, D.M. Potukuchi, D.L. Sastry, J. Magn. Magn. Mater. 407 (2016) 135–141.

[12] F.S. Li, L. Wang, J.B. Wang, Q.G. Zhou, X.Z. Zhou, H.P. Kunkel, G. Williams, J. Magn. Magn. Mater. 268 (2004) 332–339.

[13] S. Mahalakshmi, K. Srinivasa Manja, S. Nithiyanantham, J. Supercond. Nov. Magnetism 28 (2015) 3093–3098.

[14] S. Prabahar, M. Dhanam, J. Cryst. Growth 285 (2005) 41–48.

[15] T. Kavetskyy, O. Shpotyuk, M. Popescu, A. Lorinczi, F. Sava, J. Optoelectron. Adv. Mater. 9 (2007) 3079.

[16] Kunal B. Modi, Suraj J. Shah, Chetan R. Kathad, Devangi K. Sonigra, Hardik P. Parmar, Kamlakar M. Jadhav, Adv. Mater. Res. 1141 (2016) 147–152.

[17] B.D. Cullity, Introduction to Magnetic Materials, Addison Wesley, Reading, MA, 1972, p. 141.

[18] M.A. Gabal, Y.M. Al Angari, Mater. Chem. Phys. 118 (2009) 153.

[19] S.S. Jadhav, S.E. Shirsath, B.G. Toksha, S.M. Patange, S.J. Shukla, K.M. Jadhav, Int. J. Mod. Phys. 23 (2009) 5629.

[20] W. Yongfei, L. Qiaoling, Z. Cunrui, J. Hongxia, J. Alloy. Comp. 467 (2009) 284–287.

[21] M. Ul-Islam, T. Abbas, M.U. Rana, Int. J. Mod. Phys. B 20 (2008) 725–735.

[22] R.D. Waldron, Phys. Rev. 99 (1955) 1727.

[23] M.A. Almessiere, S. Dabagh, Y. Slimani, K. Chaudhary, J. Ali, A. Baykal, J. Inorg. Organomet. Polym. 28 (2018) 942–953.

[24] M.A. Gabal, J. Magn. Magn. Mater. 321 (2009) 3144–3148.

[25] S.P. Waghmare, D.M. Borikar, K.G. Rewatkar, Mater. Today: Proc. 4 (2017) 11866–11872.

[26] I.H. Gul, A.Z. Abbasi, F. Amin, M. Anis-ur-Rehman, A. Maqsood, J. Magn. Magn. Mater. 311 (2007) 494.

[27] D.R. Mane, D.D. Birajdar, S.E. Shirsath, R.A. Telugu, R.H. Kadam, Phys. Status Solidi A 207 (2010) 2355–2363.

[28] B.D. Cullity, Introduction of Magnetic Materials, Addison-Wesley Publishing Company, Indiana, 1972.

[29] L.M. Thorat, J.Y. Patil, D.Y. Nadargi, U.R. Ghodake, R.C. Kambale, S. S. Suryavanshi, J. Adv. Ceram. 7 (2018) 207–217.

[30] Talwinder Kaur, Barjinder Kaur, Bilal H. Bhat, Sachin Kumar, A.K. Srivastava, Physica B 456 (2015) 206–212.

[31] X. Li, X. Cao, L. Xu, L. Liu, Y. Wang, C. Meng, Z. Wang, J. Alloy. Comp. 657 (2016) 90–94.

[32] Vineeta Shukla, Nanoscale Adv. 1 (2019) 1640–1671.

[33] K. Cherif, A. Belkahla, J. Dhahri, J. Alloy. Comp. 777 (2019) 358–363.

[34] W.R. Agami, Physica B 534 (2018) 17–21.

[35] M.A. Ali, M.M. Uddin, M.N.I. Khan, F.-U.-Z. Chowdhury, S.M. Haque, J. Magn. Magn. Mater. 424 (2017) 148–154.

[36] Kavita Verma, Ashwini Kumar, et al., Curr. Appl. Phys. 13 (2013) 467–473.

[37] U.R. Ghodake, RahulC. Kambale, S.S. Suryavanshi, Ceram. Int. 43 (2017) 1129–1134.